

Winding number and optical conductivity of multi-Weyl semimetals

Seongjin Ahn¹, E. J. Mele^{2,*} and Hongki Min^{1,2†}

¹ *Department of Physics and Astronomy, Seoul National University, Seoul 08826, Korea and*

² *Department of Physics and Astronomy, University of Pennsylvania, Philadelphia, PA 19104, USA*

(Dated: August 18, 2022)

Multi-Weyl semimetals are a new type of Weyl semimetals which have anisotropic non-linear energy dispersion and a topological charge larger than one, thus exhibiting a unique quantum response. Using a unified lattice model we calculate the optical conductivity numerically in the multi-Weyl semimetal phase and in its neighboring gapped states, and obtain the characteristic frequency dependence of each phase analytically using a continuum model. The frequency dependence of longitudinal and transverse optical conductivities obeys scaling relations that are derived from the winding number of the parent multi-Weyl semimetal phase and can be used to distinguish these electronic states of matter.

Introduction — A Weyl semimetal (WSM) is a gapless topological state of matter possessing \mathbf{k} -space singularities where its valence and conduction bands contact at a point. This singularity is a \mathbf{k} -space monopole providing a quantized source or sink of a Berry's flux and can occur only in materials in which either time reversal symmetry or inversion symmetry is broken. In the prototypical WSM a twofold band degeneracy at the Weyl point is broken linearly in momentum in all directions and the node is characterized by chirality ± 1 . A transition to an insulating phase is possible only if Weyl nodes with opposite chirality pairwise merge and annihilate. The gapped phase produced by this merger can be in a normal insulating state or a topological quantum anomalous Hall state. The linear dispersion around the Weyl point has important consequences for the low frequency optical properties which has been explored theoretically and used experimentally as an experimental fingerprint of the topological state [1–9].

A \mathbf{k} -space merger of Weyl points with the *same* chirality produces a new type of Weyl semimetal, referred to as a multi-Weyl semimetal (m-WSM) [10, 11]. In these states the merger of the nodes is robust if it is protected by a point group symmetry. The low energy dispersion can then be characterized by double (triple) Weyl nodes with linear dispersion along one symmetry direction and quadratic (cubic) dispersion along the remaining two directions. Because of the change in topological nature, the enhancement of the density of states, the anisotropic non-linear energy dispersion and a modified spin-momentum locking structure, these states will have optical and transport signatures that distinguish them from elementary WSM's.

In this paper, we report calculations of the optical conductivity in m-WSMs, and analyze its characteristic frequency dependence in the semimetallic state and in nearby insulating states focusing on the effects of chirality, lattice regularization and phase transitions. We

study how the optical conductivity changes for these different phases using a unified lattice model in which the model parameters are varied, and obtain the characteristic frequency dependence analytically using a low energy continuum model. We find that the results can be clearly distinguished from the low-frequency electrodynamics of elementary WSMs by its low-energy frequency dependence which is determined by the winding number of the m-WSM phase.

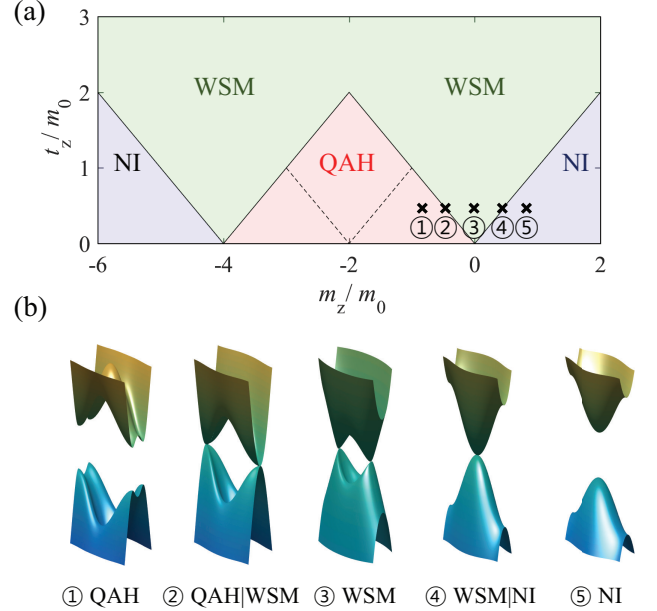


FIG. 1: (a) Phase diagrams of $J = 2$ lattice models on t_z/m_0 and m_z/m_0 plane and (b) evolution of the energy band structure from 3D quantum anomalous Hall (QAH) to normal insulator (NI) phase. Here we use several values of m_z/m_0 corresponding to different phases indicated by circled numbers in the phase diagram. QAH|WSM and WSM|NI denote the transition phase between 3D QAH and WSM, and WSM and NI, respectively. The phase diagram for $J = 1$ has similar shape but has a different phase boundary between the WSM and 3D QAH represented by the dashed line [12].

*Electronic address: mele@physics.upenn.edu

†Electronic address: hmin@snu.ac.kr

Model — The low-energy effective Hamiltonian for m-WSMs of order J near a single Weyl point can be de-

scribed by the Hamiltonian:

$$H_J = \varepsilon_0 \left(\tilde{k}_-^J \sigma_+ + \tilde{k}_+^J \sigma_- \right) + \hbar v_z k_z \sigma_z \quad (1)$$

where $\tilde{k}_\pm = k_\pm/k_0$ with $k_\pm = k_x \pm i k_y$, $\sigma_\pm = \frac{1}{2}(\sigma_x \pm i\sigma_y)$, and σ are Pauli matrices acting in the space of two bands that contact at the Weyl point. Here v_z is the effective velocity along the k_z direction, and k_0 and ε_0 are material dependent parameters in units of momentum and energy, respectively. For simplicity, we assumed the axial symmetry around the k_z -axis. Note that the eigenenergies of the Hamiltonian are given by $\varepsilon_\pm = \pm \sqrt{\varepsilon_0^2 \tilde{k}_\parallel^2 + (\hbar v_z k_z)^2}$ where $\tilde{k}_\parallel = \sqrt{\tilde{k}_x^2 + \tilde{k}_y^2}$.

Let us consider a lattice model which shows at some parameter range the m-WSM phase described by Eq. (1). A simple lattice model for the Weyl semimetals with $J = 1$ is given by [12–14]

$$\begin{aligned} H_1 &= t_x \sin(k_x a) \sigma_x + t_y \sin(k_y a) \sigma_y + M_z \sigma_z, \\ M_z &= m_z - t_z \cos(k_z a) + m_0 [2 - \cos(k_x a) - \cos(k_y a)], \end{aligned} \quad (2)$$

where a is the lattice spacing, and $t_{x,y,z}$, m_z and m_0 are material dependent parameters. Similarly, we can generalize the above lattice model in Eq. (2) to $J = 2$ so that near the Weyl points the low-energy Hamiltonian reduces to the form of Eq. (1) [15]:

$$\begin{aligned} H_2 &= t_x [\cos(k_y a) - \cos(k_x a)] \sigma_x \\ &+ t_y \sin(k_x a) \sin(k_y a) \sigma_y + M_z \sigma_z. \end{aligned} \quad (3)$$

Depending on the model parameters, the Hamiltonian in Eqs. (2) and (3) show various phases such as normal insulators (NIs), Weyl semimetals (WSMs), and 3D quantum anomalous Hall (QAH) states, as seen in Fig. 1 with corresponding energy band structures. The phase diagram for $J = 2$ has similar shape with that for $J = 1$ [12], but because of the change in the electronic structure, optical properties in the m-WSMs show strong dependence on their chirality.

For the continuum model corresponding to each phase, we choose the parameter range where Weyl nodes arise at $(k_x, k_y) = (0, 0)$. Other choice of parameter ranges give fundamentally identical settings. Using the $\mathbf{k} \cdot \mathbf{p}$ method, we can write a generic continuum model for various phases as

$$H = \varepsilon_0 \left(\tilde{k}_-^J \sigma_+ + \tilde{k}_+^J \sigma_- \right) + M_z \quad (4)$$

where the mass term M_z is given by [16]

$$M_z \approx \hbar v_z q_z + \alpha + \beta q_z^2 + \gamma (k_x^2 + k_y^2). \quad (5)$$

Here we set $\gamma = \frac{m_0 a^2}{2} > 0$ except for the WSM phase with $\gamma = 0$. Note that for the NI phase and at the transition between the NI and WSM phases (NI|WSM), $\alpha = m_z - t_z$ and $\beta = \frac{t_z a^2}{2}$, whereas for the 3D QAH phase and at the transition between the WSM and 3D QAH phases

(WSM|QAH), $\alpha = m_z + t_z$ and $\beta = -\frac{t_z a^2}{2}$. Thus, for each phase, we find

NI	:	$q_z = k_z;$	$v_z = 0;$	$\alpha, \beta > 0,$
NI WSM	:	$q_z = k_z;$	$v_z = 0;$	$\alpha = 0, \beta > 0,$
WSM	:	$q_z = k_z \mp b;$	$v_z \neq 0;$	$\alpha = \beta = 0,$
WSM QAH	:	$q_z = k_z \mp \frac{\pi}{a};$	$v_z = 0;$	$\alpha = 0, \beta < 0,$
QAH	:	$q_z = k_z \mp \frac{\pi}{a};$	$v_z = 0;$	$\alpha, \beta < 0,$

(6)

where $\cos(ba) \equiv m_z/t_z$ with $|m_z|/t_z < 1$. For calculation, we set $k_0 = 1/a$, $t_x = t_y = 4m_0$ and $t_z = 0.5m_0$ with $m_0 > 0$, and change $-m_0 < m_z < m_0$ with other parameters fixed to induce various phases.

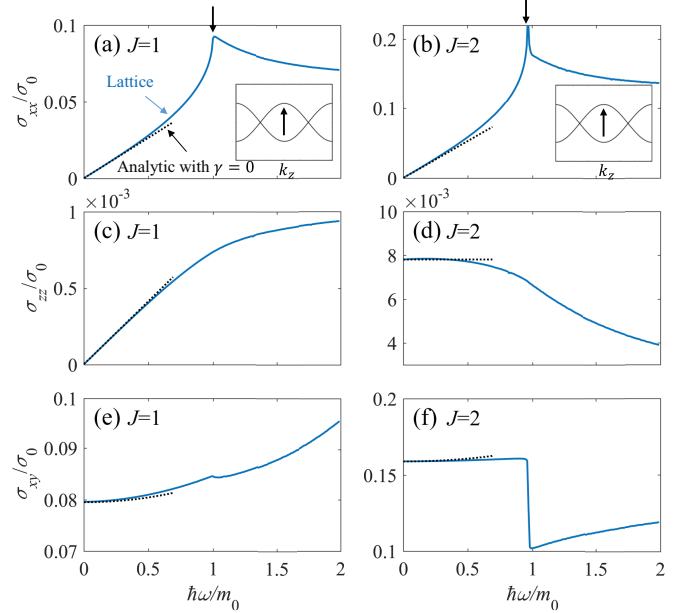


FIG. 2: Real part of (a)-(d) longitudinal and (e), (f) transverse optical conductivities in units of $\sigma_0 = \frac{e^2}{\hbar a}$ for the lattice (blue solid line) and continuum (black dotted line) models in the WSM phase. The arrows in the insets indicate interband transitions corresponding to kink structures in $\sigma_{xx}(\omega)$ and $\sigma_{xy}(\omega)$. Here $m_z/m_0 = 0$, $b = 0.5\pi/a$ and $k_c = \pi/a$ are used for calculation.

Optical conductivity — The Kubo formula for the optical conductivity in the non-interacting limit can be expressed as [17]

$$\begin{aligned} \sigma_{ij}(\omega) &= -\frac{ie^2}{\hbar} \sum_{s,s'} \int \frac{d^3k}{(2\pi)^3} \frac{f_{s,\mathbf{k}} - f_{s',\mathbf{k}}}{\varepsilon_{s,\mathbf{k}} - \varepsilon_{s',\mathbf{k}}} \\ &\times \frac{M_i^{ss'}(\mathbf{k}) M_j^{s's}(\mathbf{k})}{\hbar\omega + \varepsilon_{s,\mathbf{k}} - \varepsilon_{s',\mathbf{k}} + i0^+} \end{aligned} \quad (7)$$

where $i, j = x, y, z$, $f_{s,\mathbf{k}} = 1/[1 + e^{(\varepsilon_{s,\mathbf{k}} - \mu)/k_B T}]$ is the Fermi distribution function, μ is the chemical potential and $M_i^{ss'}(\mathbf{k}) = \langle s, \mathbf{k} | \hbar \hat{v}_i | s', \mathbf{k} \rangle$ with the velocity operator \hat{v}_i obtained from the relation $\hat{v}_i = \frac{1}{\hbar} \frac{\partial \hat{H}}{\partial k_i}$.

In the following we consider only the undoped case with $\mu = 0$. In the clean limit at zero temperature, the

real part of the longitudinal optical conductivity for m-WSMs within the continuum model is given by [16]

$$\sigma_{xx}(\omega) = \frac{g_N}{24\pi} \frac{J e^2}{\hbar v_z} \omega, \quad (8a)$$

$$\sigma_{zz}(\omega) = \frac{g_N}{24\pi} \frac{e^2 v_z}{\hbar v_z^2} A_{zz}^{\text{WSM}} \left(\frac{\omega}{\omega_0} \right)^{\frac{2}{J}-1} \omega_0, \quad (8b)$$

where $g_N = 2$ is the number of nodes, $\varepsilon_0 = \hbar\omega_0 = \hbar v_{\parallel} k_0$, and $A_{zz}^{\text{WSM}} = \frac{3\sqrt{\pi}\Gamma(\frac{J}{2})}{4J\Gamma(\frac{J}{2}+\frac{3}{2})}$. For $J = 1$, $A_{zz}^{\text{WSM}}|_{J=1} = 1$ and the result in Eq. (8) reduces to that of conventional Weyl semimetals. Note that $\sigma_{xx}(\omega) \propto J\omega$ while $\sigma_{zz} \propto \omega^{\frac{2}{J}-1}$ exhibiting the chirality dependent power-law exponents in frequencies.

Next, consider the real part of the Hall or transverse optical conductivity. Note that a sign change of M_z in the Brillouin zone can produce a nontrivial state that supports a Hall effect in the k_x - k_y plane for a fixed k_z . We therefore focus only on the in-plane off-diagonal part $\sigma_{xy}(\omega)$. If two Weyl nodes with opposite chirality are located at $\pm \mathbf{b} = \pm b\hat{\mathbf{z}}$, the real part of the Hall conductivity up to second order in ω is given by

$$\sigma_{xy}(\omega) = J\chi \frac{e^2}{\hbar} \left(\frac{b}{2\pi^2} + \frac{1}{24\pi^2 v_z^2} \frac{b}{k_c^2 - b^2 \omega^2} \right) \quad (9)$$

where k_c is the cutoff along the k_z direction. Here χ represents the right-handed/left-handed chirality which has $\chi = \pm 1$ if the node with positive chirality is at $\pm b\hat{\mathbf{z}}$ and the other at $\mp b\hat{\mathbf{z}}$. Note that the Hall conductivity for m-WSMs is given by J times that for $J = 1$ Weyl semimetals, thus their surface states could be manifested by J Fermi arcs connecting the two Weyl nodes.

Figure 2 shows calculated optical conductivities for $J = 1$ and $J = 2$ lattice and continuum models, respectively. At low frequencies, the lattice models are approximated by the corresponding low energy model in Eq. (1), thus $\sigma_{xx}(\omega)$ and $\sigma_{zz}(\omega)$ from the lattice and continuum models are in good agreement. As frequency increases, however, optical conductivities deviate from the continuum model and show a kink structure in $\sigma_{xx}(\omega)$ and $\sigma_{xy}(\omega)$ at $\hbar\omega = 2|m_z - t_z|$ due to interband transitions between states around the van Hove singularity [8], as shown in the insets to (a) and (b).

For the NI phase ($\alpha > 0$) and 3D QAH phase ($\alpha < 0$), we obtain the leading-order ω dependence of longitudinal optical conductivities analytically assuming $\gamma = 0$ in the vicinity of $\hbar\omega = 2|\alpha|$:

$$\sigma_{xx}(\omega) \sim (\hbar\omega - 2|\alpha|)^{\frac{1}{2}} \Theta(\hbar\omega - 2|\alpha|), \quad (10a)$$

$$\sigma_{zz}(\omega) \sim (\hbar\omega - 2|\alpha|)^{\frac{1}{J}+\frac{3}{2}} \Theta(\hbar\omega - 2|\alpha|). \quad (10b)$$

The full analytic results including higher order corrections in ω can be found in the Supplemental Material [16]. Note that similarly as in the WSM phase, the $\sigma_{xx}(\omega)$ has the same ω dependence regardless of the chirality index

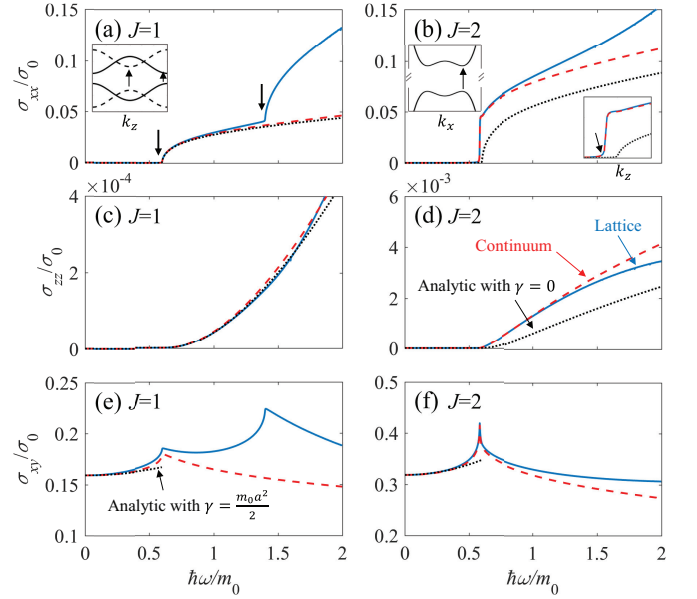


FIG. 3: Real part of (a)-(d) longitudinal and (e), (f) transverse optical conductivities in the 3D QAH phase for the lattice model (blue solid line), the continuum model (red dashed line), and the analytic results (black dotted line). For the longitudinal (transverse) conductivities, the analytic results are obtained for $\gamma = 0$ ($\gamma = \frac{m_0 a^2}{2}$). Solid (dashed) lines in the inset to (a) represent the energy dispersion for $J = 1$ along the k_z direction with $k_x = 0$ ($k_x = \frac{\pi}{a}$) and $k_y = 0$. The left inset to (b) represents the energy dispersion for $J = 2$ along the k_x direction with $k_z = \frac{\pi}{a}$ and $k_y = 0$, and the right inset to (b) shows an enlarged view in $\sigma_{xx}(\omega)$ near the interband transition. Arrows in the insets indicate interband transitions corresponding to kink structures appearing in σ_{xx} and σ_{xy} . Note that for $J = 2$, a Mexican hat structure appears in the energy dispersion exhibiting a shifted interband peak with respect to the $\gamma = 0$ result. Here $m_z/m_0 = -0.8$ and $k_c = \pi/a$ are used for calculation.

J , while $\sigma_{zz}(\omega)$ has different power-law exponents depending on J .

The transverse optical conductivities in the NI and 3D QAH phases up to second order in ω are given by

$$\sigma_{xy}(\omega) \approx \frac{e^2}{\hbar} [A_{xy} + B_{xy}\omega^2] \quad (11)$$

where

$$A_{xy}|_{J=1} = \xi \frac{k_c}{2\pi^2}, \quad (12a)$$

$$A_{xy}|_{J=2} = \frac{k_c}{2\pi^2} \left(\frac{\gamma k_0^2}{\sqrt{(\gamma k_0^2)^2 + \varepsilon_0^2}} \mp 1 \right), \quad (12b)$$

and k_c is the cutoff along the k_z direction. Here \mp refer to the NI phase and 3D QAH phase, respectively, and $\xi = 0$ ($\xi = 1$) for the NI (3D QAH) phase. The expression for B_{xy} can be found in the Supplemental Material [16]. Note that for the transverse optical conductivities, we present analytic results with non-zero γ .

Figure 3 shows calculated optical conductivities for $J = 1$ and $J = 2$ lattice and continuum models in the 3D QAH phase. If $\gamma = 0$, the energy gap with the size of $2|\alpha|$ for both NI and 3D QAH phases leads to zero conductivity for frequencies $\hbar\omega < 2|\alpha|$ due to the Pauli blocking. Because of non-zero γ , a Mexican hat structure appears in the 3D QAH phase (but not in the NI phase) if $\alpha < \alpha_c = -\frac{\varepsilon_0^2}{2\gamma k_0^2}$ for $J = 1$, and if $\alpha < 0$ for $J = 2$ exhibiting a shifted interband peak with respect to the $\gamma = 0$ result [16]. Note that for the $J = 1$ lattice model in the 3D QAH phase, additional kink structure appears at $\hbar\omega = 2|m_z - t_z + 2m_0|$ due to interband transitions at local minima $(k_x, k_y, k_z) = (\pm\frac{\pi}{a}, 0, 0), (0, \pm\frac{\pi}{a}, 0)$, as seen in Fig. 3(a). The continuum model longitudinal conductivities agree well with the lattice results both qualitatively and quantitatively whereas analytic results with zero γ for the longitudinal conductivities agree only qualitatively with the lattice results. Note that the analytic results for the longitudinal conductivities presented here are obtained assuming $\gamma = 0$ for simplicity, which is valid when the effect of the band distortion associated with nonzero γ is small ($m_0 \ll t_x, t_y$).

Two remarks are in order. First, the results in Eq. (12) show that the static Hall conductivity $\sigma_{xy}(\omega = 0)$ in the NI phase is nonzero for $J = 2$ in contrast to the corresponding lattice result whereas the static Hall conductivity in the 3D QAH phase which characterizes the topological state of the system seems not to be quantized for $J = 2$ because $A_{xy}^{\text{QAH}}|_{J=2}$ is an arbitrary number depending on material dependent parameters such as γ and ε_0 . This occurs because the continuum model can give only the difference in the Hall conductivity between two different phases. Thus $\sigma_{xy}(\omega = 0)$ in the transverse conductivity computed in this model is not directly experimentally measurable but the difference in this quantity between different electronic states is. Since the static part of the Hall conductivity in the NI phase is zero, the corresponding continuum model result obtained in the NI phase should be subtracted from those obtained in other phases so that the static Hall conductivity becomes zero in the NI phase, whereas in the 3D QAH phase $A_{xy}^{\text{QAH}}|_{J=2} \rightarrow A_{xy}^{\text{QAH}}|_{J=2} - A_{xy}^{\text{NI}}|_{J=2} = \frac{2k_c}{2\pi^2}$ recovering a quantized value. (In general, the static Hall conductivity is proportional to the chirality so that $A_{xy}^{\text{QAH}}|_J \rightarrow \frac{Jk_c}{2\pi^2}$.) Thus, when this residual conductivity is subtracted from the continuum model results for other insulating phases, the results are consistent with those obtained from the lattice model. Continuum model Hall conductivities presented in the figures throughout the paper (both numerical and analytic results) have this residual conductivity subtracted. In this sense, we choose the momentum cutoff along the k_z direction as $k_c = \pi/a$ so that the properly subtracted static Hall conductivity in the 3D QAH phase has the same quantized value as in the lattice model. Along the k_x and k_y directions, we set a large enough momentum cutoff ($\sim 10^3/a$). Second, $B_{xy}|_{J=1}$ and $B_{xy}|_{J=2}$ are not zero, indicating that the system is a

dynamical Hall insulator even in the NI phase. Deep inside the NI (3D QAH) phase, however, $\lim_{\alpha \rightarrow \pm\infty} B_{xy} = 0$ thus the system becomes a trivial insulator (quantized Hall insulator) at finite frequencies.

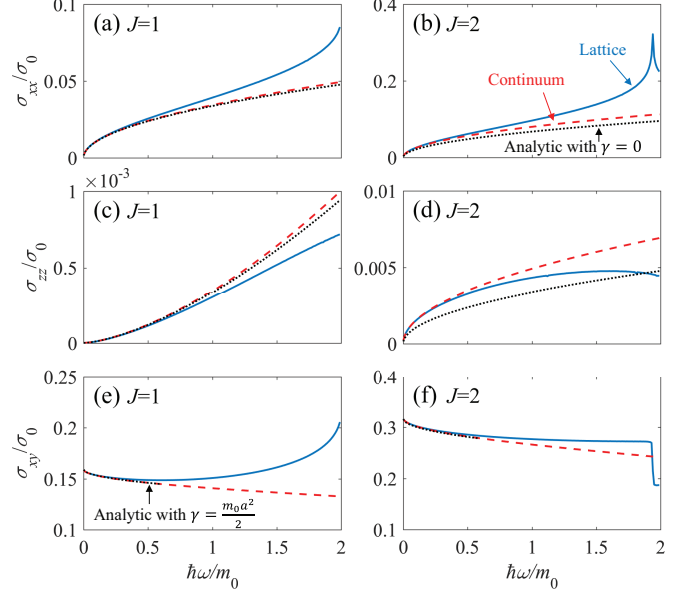


FIG. 4: Real part of (a)-(d) longitudinal and (e), (f) transverse optical conductivities at the transition between the 3D QAH and WSM phases for the lattice model (blue solid line), the continuum model (red dashed line), and the analytic results (black dotted line). For the longitudinal (transverse) conductivities, the analytic results are obtained for $\gamma = 0$ ($\gamma = \frac{m_0 a^2}{2}$). Here $m_z/m_0 = -0.5$ and $k_c = \pi/a$ are used for calculation.

At the transition point between the WSM and NI phases or between the WSM and 3D QAH phases, the longitudinal (transverse) optical conductivities obtained assuming zero (non-zero) γ are given by

$$\sigma_{xx}(\omega) = \frac{e^2}{\hbar} A_{xx} (\hbar\omega)^{\frac{1}{2}}, \quad (13a)$$

$$\sigma_{zz}(\omega) = \frac{e^2}{\hbar} A_{zz} (\hbar\omega)^{\frac{2}{J}-\frac{1}{2}}, \quad (13b)$$

$$\sigma_{xy}(\omega) = \xi \sigma_{xy}^{\text{QAH}} + \frac{e^2}{\hbar} [A_{xy}^{\text{NI}} + B_{xy} \omega^\nu], \quad (13c)$$

where $\sigma_{xy}^{\text{QAH}} = \frac{e^2}{\hbar} \frac{Jk_c}{2\pi^2}$ and A_{xy}^{NI} is a residual conductivity in Eq. (12) for the NI phase that should be subtracted to get an absolute conductivity which is consistent with the lattice model result. The expressions for A_{xx} and A_{zz} can be found in the Supplemental Material [16]. Here the exponent $\nu \approx 0.5$ is found numerically for $J = 1, 2$ with a frequency independent coefficient B_{xy} . Note that longitudinal conductivities for both transition points are identical (within $\gamma = 0$ approximation), whereas Hall conductivities have different static values with a difference given by σ_{xy}^{QAH} .

Discussion — Recently, Huang *et al.* [18] demonstrated that strontium silicide (SrSi₂) hosts double Weyl

nodes with a chirality $J = 2$. The effective Hamiltonian which describes one of the Weyl nodes with the chirality $J = 2$ in SrSi_2 resembles that of bilayer graphene with the interlayer hopping replaced by the spin-orbit coupling Δ connecting the two $J = 1$ Weyl Hamiltonians. If we assume $\mu = 0$, at low frequencies the optical conductivity for SrSi_2 behaves as that of the $J = 2$ Weyl semimetals showing $\sigma_{xx} \sim \omega$ and $\sigma_{zz} \sim \omega^0$ dependence, whereas at high frequencies, the optical conductivity shows the result of the two copies of the $J = 1$ Weyl semimetals exhibiting a linear ω dependence in σ_{xx} and σ_{zz} . At intermediate frequencies, there appear kink structures at frequencies comparable to the energy scales of interband transitions determined by Δ . Note that in SrSi_2 , the Weyl point is not actually located at $\mu = 0$, thus the longitudinal conductivity in real SrSi_2 will give additional features of the Pauli blocking for interband transitions and the Drude peak for intraband transitions (in addition to contributions from other Weyl nodes).

In summary, we study optical properties of m-WSMs in semimetallic and nearby insulating phases focusing

on the frequency dependence of optical conductivity. We demonstrate that the optical conductivities $\sigma_{xx}(\omega)$, $\sigma_{zz}(\omega)$ and $\sigma_{xy}(\omega)$ show the characteristic frequency dependence that strongly varies according to the chirality and phase of the system, thus can be used as a spectroscopic signature of m-WSMs.

Acknowledgments

This research was supported by Basic Science Research Program through the National Research Foundation of Korea (NRF) funded by the Ministry of Education under Grant No. 2015R1D1A1A01058071. EJM's work on this project was supported by the U.S. Department of Energy, Office of Basic Energy Sciences under award DE-FG02-ER45118. HM acknowledges travel support provided by the University Research Foundation at the University of Pennsylvania while this work was carried out.

-
- [1] Xiangang Wan, Ari M. Turner, Ashvin Vishwanath, and Sergey Y. Savrasov, Topological semimetal and Fermi-arc surface states in the electronic structure of pyrochlore iridates, *Phys. Rev. B* **83**, 205101 (2011).
 - [2] Pavan Hosur, S. A. Parameswaran, and Ashvin Vishwanath, Charge Transport in Weyl Semimetals, *Phys. Rev. Lett.* **108**, 046602 (2012).
 - [3] Phillip E. C. Ashby and J. P. Carbotte, Chiral anomaly and optical absorption in Weyl semimetals, *Phys. Rev. B* **89**, 245121 (2014).
 - [4] A. B. Sushkov, J. B. Hofmann, G. S. Jenkins, J. Ishikawa, S. Nakatsuji, S. Das Sarma, and H. D. Drew, Optical evidence for a Weyl semimetal state in pyrochlore $\text{Eu}_2\text{Ir}_2\text{O}_7$, *Phys. Rev. B* **92**, 241108(R) (2015).
 - [5] R. Y. Chen, S. J. Zhang, J. A. Schneeloch, C. Zhang, Q. Li, G. D. Gu, and N. L. Wang, Optical spectroscopy study of the three-dimensional Dirac semimetal ZrTe_5 , *Phys. Rev. B* **92**, 075107 (2015).
 - [6] B. Xu, Y. M. Dai, L. X. Zhao, K. Wang, R. Yang, W. Zhang, J. Y. Liu, H. Xiao, G. F. Chen, A. J. Taylor, D. A. Yarotski, R. P. Prasankumar, and X. G. Qiu, Optical spectroscopy of the Weyl semimetal TaAs, *Phys. Rev. B* **93**, 121110(R) (2016).
 - [7] C. J. Tabert, J. P. Carbotte, and E. J. Nicol, Optical and transport properties in three-dimensional Dirac and Weyl semimetals, *Phys. Rev. B* **93**, 085426 (2016).
 - [8] C. J. Tabert and J. P. Carbotte, Optical conductivity of Weyl semimetals and signatures of the gapped semimetal phase transition, *Phys. Rev. B* **93**, 085442 (2016).
 - [9] D. Neubauer, J. P. Carbotte, A. A. Nateprov, A. Lhle, M. Dressel, and A. V. Pronin, Interband optical conductivity of the [001]-oriented Dirac semimetal Cd_3As_2 , *Phys. Rev. B* **93**, 121202(R) (2016).
 - [10] G. Xu, H. Weng, Z. Wang, X. Dai, and Z. Fang, Chern Semimetal and the Quantized Anomalous Hall Effect in HgCr_2Se_4 and SrSi_2 , *Phys. Rev. Lett.* **107**, 186806 (2011).
 - [11] C. Fang, M. J. Gilbert, X. Dai, and B. A. Bernevig, Multi-Weyl Topological Semimetals Stabilized by Point Group Symmetry, *Phys. Rev. Lett.* **108**, 266802 (2012).
 - [12] Chui-Zhen Chen, Juntao Song, Hua Jiang, Qing-feng Sun, Ziqiang Wang, and X.C. Xie, Disorder and Metal-Insulator Transitions in Weyl Semimetals, *Phys. Rev. Lett.* **115**, 246603 (2015).
 - [13] P. Delplace, J. Li and D. Carpentier, Topological Weyl semi-metal from a lattice model, *EPL* **97**, 67004 (2012).
 - [14] Ari M. Turner and Ashvin Vishwanath, Beyond Band Insulators: Topology of Semi-metals and Interacting Phases, arXiv:1301.0330 (2013).
 - [15] Shao-Kai Jian and Hong Yao, Correlated double-Weyl semimetals with Coulomb interactions: Possible applications to HgCr_2Se_4 and SrSi_2 , *Phys. Rev. B* **92**, 045121 (2015).
 - [16] See Supplemental Material for details of the continuum model and corresponding energy dispersion at each phase, and the analytic expressions for optical conductivities.
 - [17] Gerald D. Mahan, *Many-particle physics* (3rd ed.), Springer (2000).
 - [18] S.-M. Huang, S.-Y. Xu, I. Belopolski, C.-C. Lee, G. Chang, T.-R. Chang, B. Wang, N. Alidoust, G. Bian, M. Neupane, D. Sanchez, H. Zheng, H.-T. Jeng, A. Bansil, T. Neupert, H. Lin, and M. Z. Hasan, New type of Weyl semimetal with quadratic double Weyl fermions, *Proc. Natl. Acad. Sci.* **113**, 1180 (2016).

Supplemental Material: Winding number and optical conductivity of multi-Weyl semimetals

Seongjin Ahn¹, E. J. Mele², and Hongki Min^{1,2}

¹ *Department of Physics and Astronomy, Seoul National University, Seoul 08826, Korea and*

² *Department of Physics and Astronomy, University of Pennsylvania, Philadelphia, PA 19104, USA*

I. CONTINUUM MODEL FOR EACH PHASE IN MULTI-WEYL SEMIMETALS

In this section, we discuss a continuum model for each phase in the phase diagram including the transition point. For calculation, we set $k_0 = 1/a$, $t_x = t_y = 4m_0$ and $t_z = 0.5m_0$ with $m_0 > 0$, and change $-m_0 < m_z < m_0$ with other parameters fixed to induce various phases.

A. WSM phase

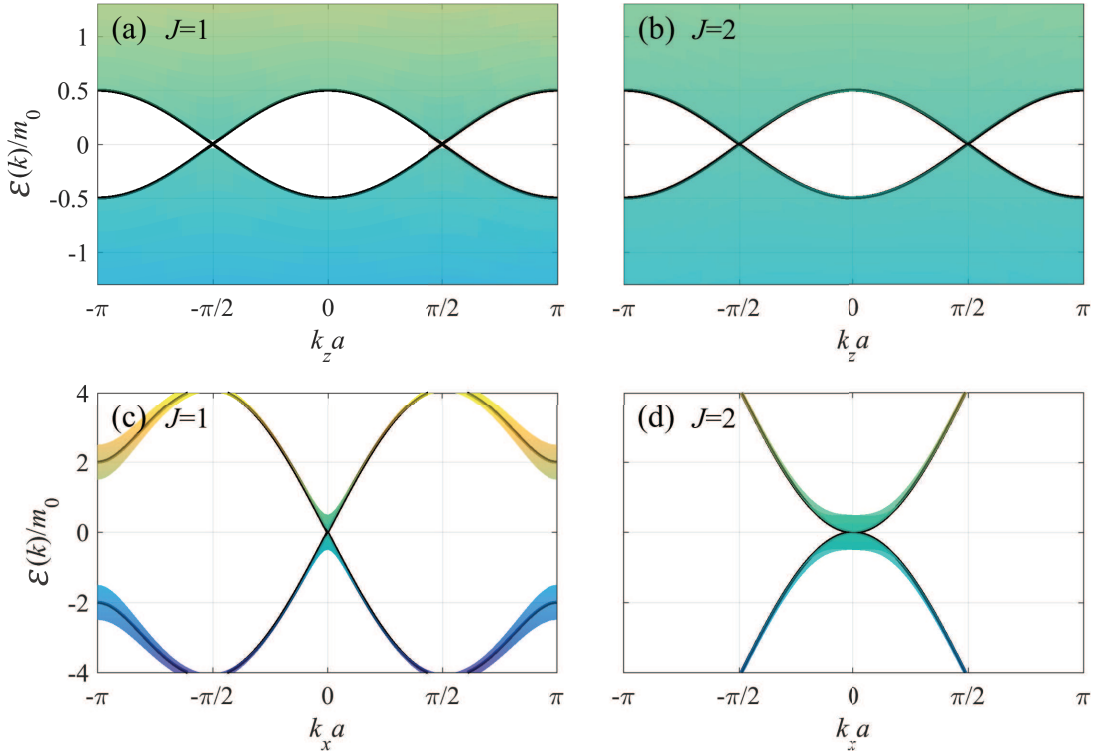


FIG. 1: Energy dispersions for $J = 1$ and $J = 2$ lattice models in the WSM phase viewed from k_z - and k_x -axis. Shaded regions represent the energy dispersions obtained by projecting them to (a), (b) k_z -axis or to (c), (d) k_x -axis at $k_y = 0$, in which each point of the dispersion is colored according to the energy scale with yellow (blue) indicating higher (lower) values. The black solid lines are added to represent the energy dispersions across the Weyl node along the (a), (b) k_z -axis with $k_x = 0$ and (c), (d) k_x -axis with $k_z = b$. Here $m_z/m_0 = 0$ and $b = 0.5\pi/a$ are used for calculation.

First, consider a continuum model for the WSM phase. For $|m_z|/t_z < 1$ with $\cos(ba) \equiv m_z/t_z$, there appear two Weyl points at $\mathbf{k} = \pm b\hat{z}$, at which the conduction and valence bands touch at zero energy. Then the Hamiltonian for $J = 1$ reduces to a form of Weyl semimetals:

$$H_1 \approx \hbar v_x k_x \sigma_x + \hbar v_y k_y \sigma_y \pm \hbar v_z q_z \sigma_z \quad (1)$$

where $q_z = k_z \mp b$, $\frac{\hbar v_x}{a} = t_x$, $\frac{\hbar v_y}{a} = t_y$ and $\frac{\hbar v_z}{a} = t_z \sin(ba)$. Similarly, for $J = 2$, the Hamiltonian H_2 reduces to Eq. (1) of the main text with $J = 2$ where $\varepsilon_0 = \frac{1}{2}t_{\parallel}(k_0 a)^2$ with $t_x = t_y \equiv t_{\parallel}$ and $\frac{\hbar v_z}{a} = t_z \sin(ba)$. Note that the

two Weyl points located at $\mathbf{k} = \pm b\hat{z}$ have opposite handedness $\chi = \pm 1$ representing the right-handed/left-handed chirality with the Chern number χJ .

Figure 1 shows the energy dispersion for $J = 1$ and $J = 2$ lattice models in the WSM phase. As shown in Eq. (1) of the main text, the energy dispersion near the Weyl point along the k_z direction with $k_x = k_y = 0$ is linear while that along the k_x - k_y directions with $k_z = 0$ is proportional to k^J . Note that there always appear multiple Weyl points in the Brillouin zone with the total chirality sum zero, and in the lattice model we are considering, there are two Weyl nodes with opposite chiralities. Between the two Weyl points, the energy dispersion becomes flat along the k_z direction at $k_x = k_y = 0$ showing a van Hove singularity, which gives rise to an interband transition peak in the optical conductivity, as shown in Fig. 2 in the main text.

B. NI phase

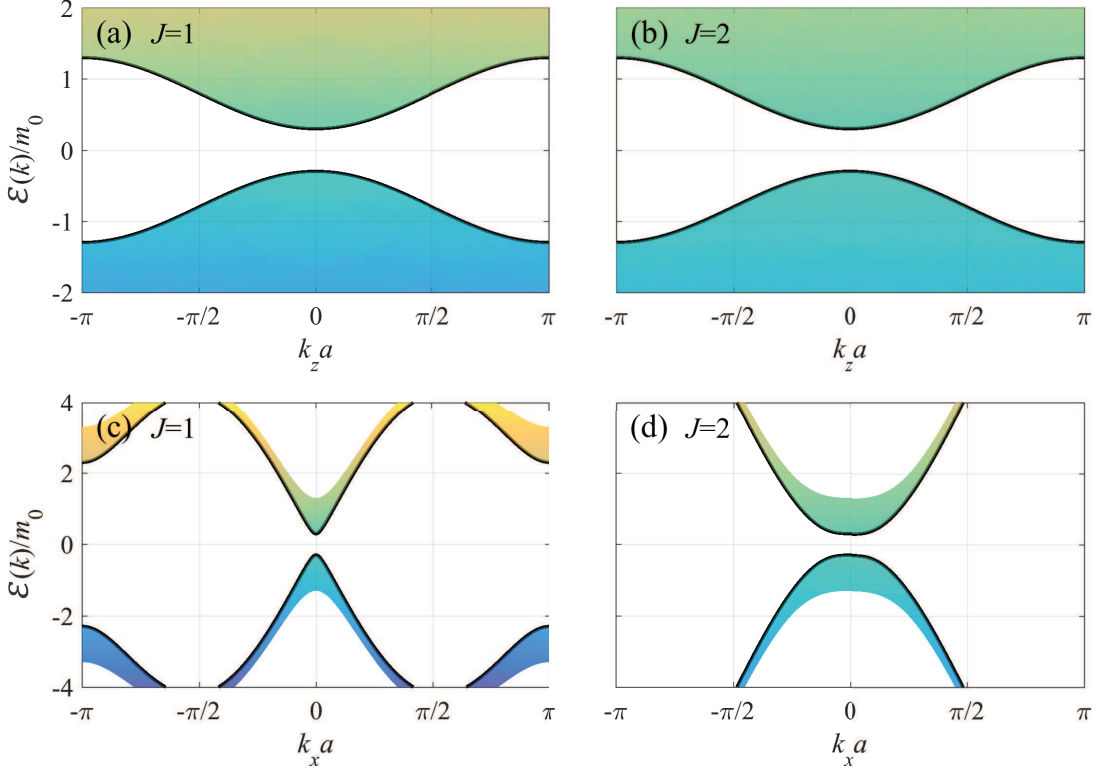


FIG. 2: Energy dispersions for (a), (c) $J = 1$ and (b), (d) $J = 2$ lattice models in the NI phase viewed from (a), (b) k_z - and (c), (d) k_x -axis with $k_y = 0$. Here $m_z/m_0 = 0.8$ is used for calculation.

For $m_z > t_z$, the mass term M_z defined in Eq. (2) of the main text remains positive throughout the Brillouin zone, thus the system is in the trivial insulator phase. Near $\mathbf{k} = (0, 0, 0)$, M_z can be approximated as

$$M_z \approx m_z - t_z + \frac{t_z a^2}{2} k_z^2 + \frac{m_0 a^2}{2} (k_x^2 + k_y^2). \quad (2)$$

Figure 2 shows the energy dispersions for $J = 1$ and $J = 2$ lattice models with an energy gap of the size of 2α where $\alpha = m_z - t_z$, which gives rise to a corresponding optical gap.

C. 3D QAH phase

For $m_z < -t_z$, the mass term M_z changes its sign in the Brillouin zone generating a non-trivial insulating phase in contrast to the case of the NI phase. Near $\mathbf{k} = (0, 0, \pm \frac{\pi}{a})$, M_z can be approximated as

$$M_z \approx m_z + t_z - \frac{t_z a^2}{2} k_z^2 + \frac{m_0 a^2}{2} (k_x^2 + k_y^2) \quad (3)$$

where $q_z = k_z \mp \frac{\pi}{a}$.

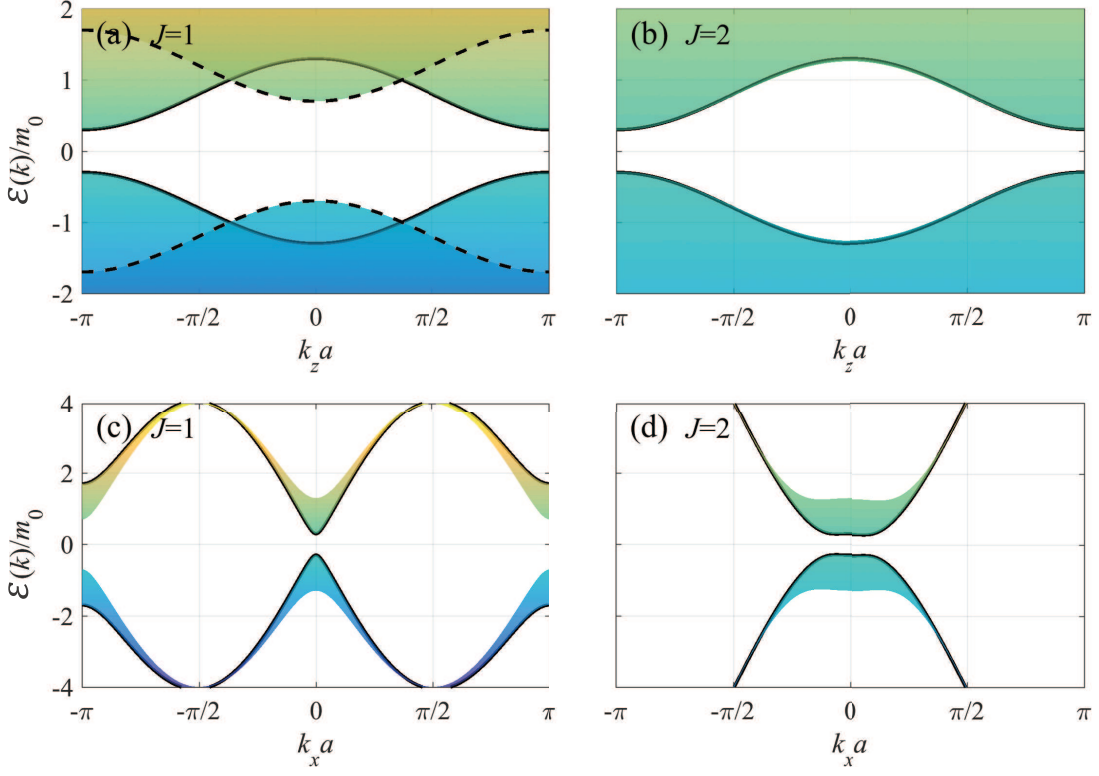


FIG. 3: Energy dispersions for (a), (c) $J = 1$ and (b), (d) $J = 2$ lattice models in the 3D QAH phase viewed from (a), (b) k_z - and (c), (d) k_x -axis with $k_y = 0$. Here $m_z/m_0 = -0.8$ is used for calculation. The dashed lines in (a) represent the energy dispersion along the k_z -axis with $k_x = \frac{\pi}{a}$ and $k_y = 0$. Note that the interband transition between the dashed bands at $k_z = 0$ corresponds to the second peak in $\sigma_{xx}(\omega)$, as shown in Fig. 3(a) in the main text.

Figure 3 shows the energy dispersion for $J = 1$ and $J = 2$ lattice models in the 3D QAH phase. Because of the negative sign of the constant term $\alpha = m_z + t_z < 0$ in M_z , the 3D QAH phase has a different gap structure compared with the NI phase. Let $\gamma = \frac{m_0 a^2}{2} > 0$. It is easy to show that for $J = 1$, if $\alpha \geq \alpha_c = -\frac{\varepsilon_0^2}{2\gamma k_0^2}$, there appears an energy gap of $2|\alpha|$ at $\mathbf{k} = (0, 0, \pm \frac{\pi}{a})$ whereas if $\alpha < \alpha_c$, there appears a Mexican hat structure with the gap of $2\sqrt{2\alpha_c\alpha - \alpha_c^2}$ away from the \mathbf{k} point. Note that in addition to $(k_x, k_y, k_z) = (0, 0, \pm \frac{\pi}{a})$, there appear local minima at $(k_x, k_y, k_z) = (\pm \frac{\pi}{a}, 0, 0)$ and $(0, \pm \frac{\pi}{a}, 0)$ in the $J = 1$ 3D QAH phase, which give additional kink structure in the optical conductivity, as shown in Fig. 3(a) in the main text. For $J = 2$, there always appear a Mexican hat structure for $\alpha < 0$ with the gap of $\frac{2|\alpha|}{\varepsilon_0(\varepsilon_0 + \Gamma)} \sqrt{\varepsilon_0^2 \Gamma^2 + (\varepsilon_0^2 + \varepsilon_0 \Gamma - \Gamma^2)^2}$ where $\Gamma = \gamma k_0^2$.

D. Transition between the WSM and NI phases

At $m_z = t_z$, near $\mathbf{k} = (0, 0, 0)$, M_z can be approximated as

$$M_z \approx \frac{t_z a^2}{2} k_z^2 + \frac{m_0 a^2}{2} (k_x^2 + k_y^2). \quad (4)$$

Figure 4 shows the energy dispersion for $J = 1$ and $J = 2$ lattice models at the transition between the WSM and NI phases. Note that the low-energy dispersion along the k_z direction with $k_x = k_y = 0$ is *quadratic* while that along the k_x - k_y directions with $k_z = 0$ is linear for $J = 1$ and quadratic for $J > 1$. As shown in the main text, the change in the energy dispersion affects the optical conductivity exhibiting different characteristic frequency dependence compared with that in the WSM or NI phase.

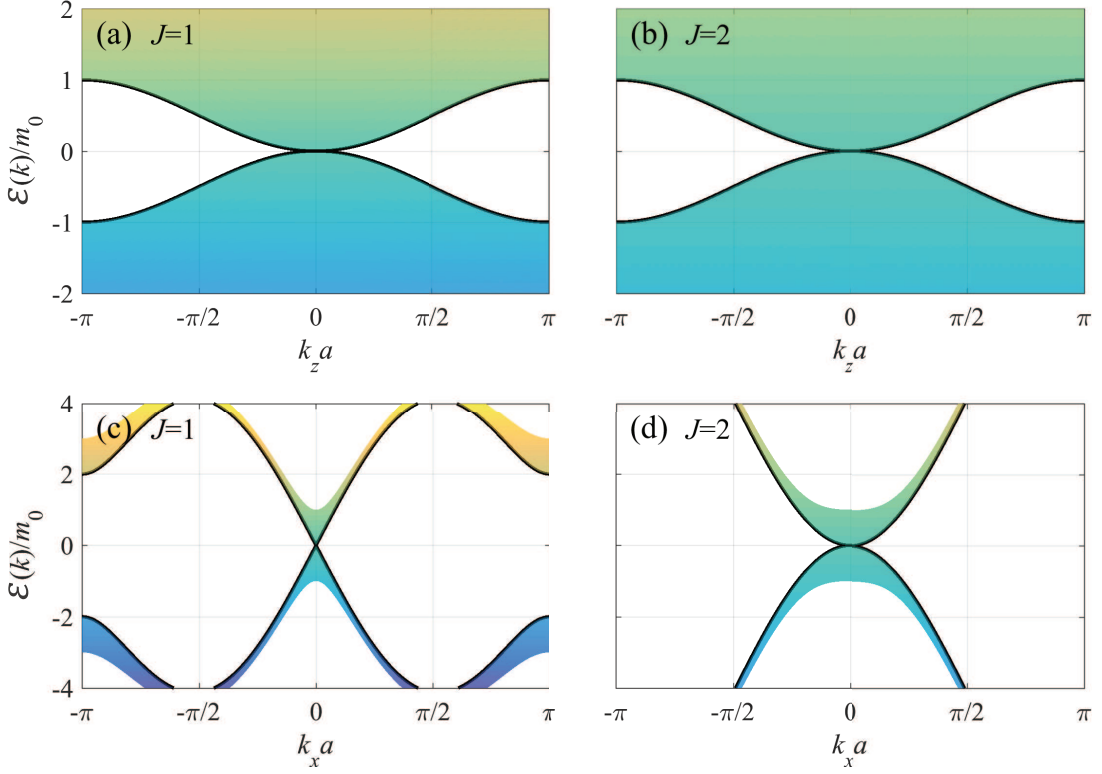


FIG. 4: Energy dispersions for (a), (c) $J = 1$ and (b), (d) $J = 2$ lattice models at the transition between the WSM and NI phases viewed from (a), (b) k_z - and (c), (d) k_x -axis with $k_y = 0$. Here $m_z/m_0 = 0.5$ is used for calculation.

E. Transition between the WSM and 3D QAH phases

At $m_z = -t_z$, near $\mathbf{k} = (0, 0, \pm \frac{\pi}{a})$, M_z can be approximated as

$$M_z \approx -\frac{t_z a^2}{2} q_z^2 + \frac{m_0 a^2}{2} (k_x^2 + k_y^2) \quad (5)$$

where $q_z = k_z \mp \frac{\pi}{a}$.

Figure 5 shows the energy dispersion for $J = 1$ and $J = 2$ lattice models at the transition between the WSM and 3D QAH phases. Note that similarly as the transition between the WSM and NI phases, the low-energy dispersion along the k_z direction with $k_x = k_y = 0$ is *quadratic* while that along the k_x - k_y directions with $q_z = 0$ is linear for $J = 1$ and quadratic for $J > 1$. The change in the energy dispersion affects the optical conductivity exhibiting different characteristic frequency dependence compared with that in the WSM or 3D QAH phase, as shown in Fig. 4 in the main text.

II. ANALYTIC EXPRESSIONS OF OPTICAL CONDUCTIVITY FOR EACH PHASE

In this section, we present detailed derivations of the optical conductivities for multi-Weyl semimetals in various phases. We consider the following continuum Hamiltonian introduced in Eq. (5) of the main text that describes various phases such as normal insulators (NIs), Weyl semimetals (WSM) and 3D quantum anomalous Hall (QAH) states, and the transition between them:

$$H = \varepsilon_0 \left[\left(\frac{k_-}{k_0} \right)^J \sigma_+ + \left(\frac{k_+}{k_0} \right)^J \sigma_- \right] + M_z \sigma_z, \quad (6)$$

$$M_z = c_1 + c_2 \left(\frac{q_z}{k_0} \right)^n + c_3 \left[\left(\frac{k_x}{k_0} \right)^2 + \left(\frac{k_y}{k_0} \right)^2 \right],$$

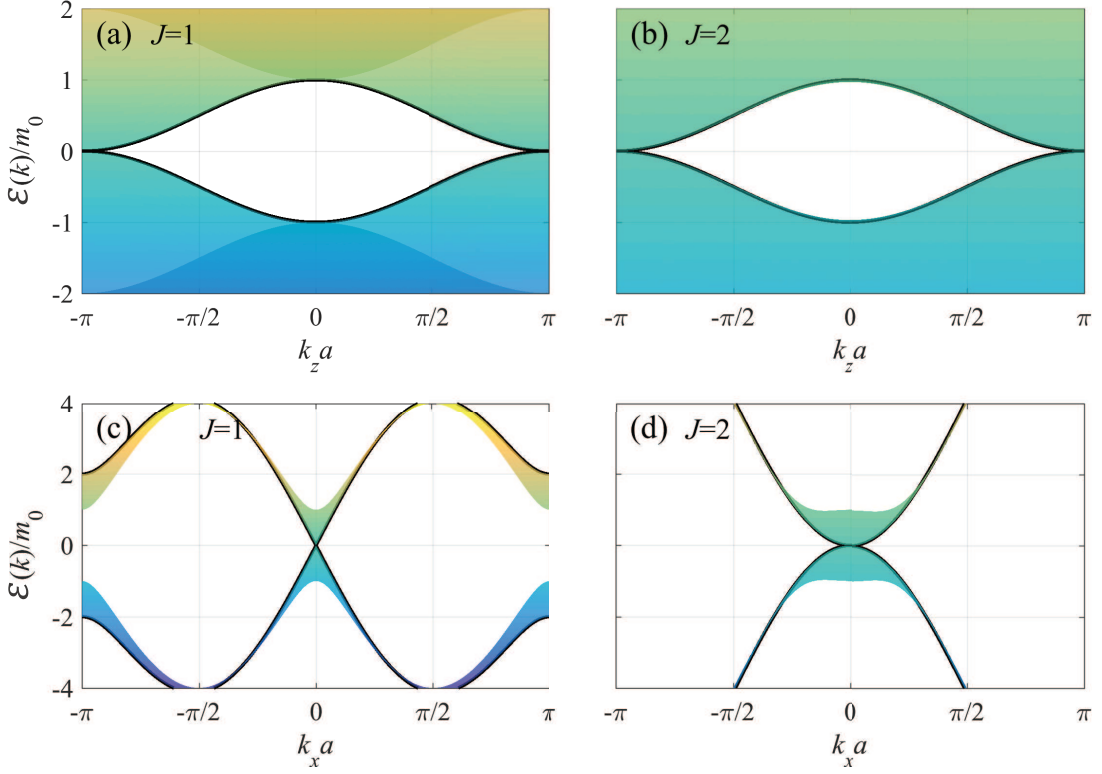


FIG. 5: Energy dispersions for (a), (c) $J = 1$ and (b), (d) $J = 2$ lattice models at the transition between the WSM and 3D QAH phases viewed from (a), (b) k_z - and (c), (d) k_x -axis with $k_y = 0$. Here $m_z/m_0 = -0.5$ is used for calculation.

where $\sigma_{\pm} = \frac{1}{2}(\sigma_x \pm i\sigma_y)$, $k_{\pm} = k_x \pm ik_y$, and q_z is the effective wavevector along the k_z direction defined in Eq. (6) of the main text. Note that for the WSM phase, $c_1 = 0$, $c_2 = \hbar v_z k_0$ and $c_3 = 0$ with $n = 1$ whereas for the insulator phases such as NI and 3D QAH, $c_1 = \alpha$, $c_2 = \beta k_0^2$ and $c_3 = \gamma k_0^2$ with $n = 2$. For the transition point, $c_1 = 0$, $c_2 = \beta k_0^2$ and $c_3 = \gamma k_0^2$ with $n = 2$.

A. Longitudinal optical conductivity

Using Eq. (7) in the main text, we can obtain optical conductivities for multi-Weyl semimetals in the non-interacting limit. Note that for the longitudinal conductivity, $M_i^{ss'}(\mathbf{k})M_i^{s's}(\mathbf{k}) = |M_i^{ss'}(\mathbf{k})|^2$ ($i = x, y, z$) is always real, thus the intraband and interband contributions of the real-part optical conductivity in the clean limit can be expressed as

$$\sigma_{ii}^{\text{intra}}(\omega) = -\frac{\pi e^2}{\hbar} \sum_{s=\pm} \int \frac{d^3k}{(2\pi)^3} \frac{\partial f_{s,\mathbf{k}}}{\partial \varepsilon_{s,\mathbf{k}}} |M_i^{ss}(\mathbf{k})|^2 \delta(\hbar\omega) \quad (7)$$

and

$$\sigma_{ii}^{\text{inter}}(\omega) = -\frac{\pi e^2}{\hbar} \int \frac{d^3k}{(2\pi)^3} \frac{f_{-, \mathbf{k}} - f_{+, \mathbf{k}}}{\varepsilon_{-, \mathbf{k}} - \varepsilon_{+, \mathbf{k}}} |M_i^{-+}(\mathbf{k})|^2 \delta(\hbar\omega + \varepsilon_{-, \mathbf{k}} - \varepsilon_{+, \mathbf{k}}) \quad (8)$$

at positive frequencies ($\omega > 0$).

Using this formula, it is straightforward to obtain the longitudinal optical conductivity for multi-Weyl semimetals. Because of the anisotropic energy dispersion, however, it is not trivial to obtain analytic expressions for the optical conductivity. In this section, we set $c_3 = 0$ (or $\gamma = 0$) for simplicity, which is valid when the effect of the band distortion associated with nonzero γ is small ($m_0 \ll t_x, t_y$). To avoid difficulties associated with anisotropic dispersions, we

consider the following coordinate transformation

$$\begin{aligned} k_x &\rightarrow k_0 \left(\frac{\rho}{\varepsilon_0} \right)^{\frac{1}{J}} \cos \phi, \\ k_y &\rightarrow k_0 \left(\frac{\rho}{\varepsilon_0} \right)^{\frac{1}{J}} \sin \phi, \\ q_z &\rightarrow k_0 \left(\frac{z}{c_2} \right)^{\frac{1}{n}}, \end{aligned} \quad (9)$$

which transforms the Hamiltonian into the following linear form:

$$H = \rho(e^{-iJ\phi}\sigma_+ + e^{iJ\phi}\sigma_-) + (c_1 + z)\sigma_z. \quad (10)$$

Note that the transformed coordinates do not cover the lower hemisphere part (i.e., $q_z < 0$) when n is an even number. We can avoid this problem by taking advantage of the inversion symmetry of the system [$H(q_z) = H(-q_z)$ for even n], allowing us to get the right result by integrating over only the positive part of q_z . In the transformed coordinates, the energy dispersion is given by $E_{\pm}(\rho, z) = \pm E(\rho, z)$ where $E(\rho, z) = \sqrt{\rho^2 + (c_1 + z)^2}$. The corresponding eigenstate is given by

$$|+; \rho, \phi, z\rangle = \begin{pmatrix} \cos \frac{\theta}{2} \\ \sin \frac{\theta}{2} e^{iJ\phi} \end{pmatrix}, \quad (11a)$$

$$|-; \rho, \phi, z\rangle = \begin{pmatrix} -\sin \frac{\theta}{2} \\ \cos \frac{\theta}{2} e^{iJ\phi} \end{pmatrix}, \quad (11b)$$

where $\theta = \tan^{-1} \left(\frac{\rho}{c_1 + z} \right)$. Note that $\cos \theta = \frac{c_1 + z}{E(\rho, z)}$ and $\sin \theta = \frac{\rho}{E(\rho, z)}$.

The Jacobian \mathcal{J} corresponding to this transformation is given by

$$\mathcal{J} = \left| \begin{array}{ccc} \frac{\partial k_x}{\partial \rho} & \frac{\partial k_x}{\partial \phi} & \frac{\partial k_x}{\partial z} \\ \frac{\partial k_y}{\partial \rho} & \frac{\partial k_y}{\partial \phi} & \frac{\partial k_y}{\partial z} \\ \frac{\partial q_z}{\partial \rho} & \frac{\partial q_z}{\partial \phi} & \frac{\partial q_z}{\partial z} \end{array} \right| = \frac{k_0^3 \left(\frac{\rho}{\varepsilon_0} \right)^{\frac{2}{J}} \left(\frac{z}{c_2} \right)^{\frac{1}{n}}}{Jn\rho z} \equiv \mathcal{J}(\rho, z). \quad (12)$$

The velocity matrices $\hat{v}_i = \frac{1}{\hbar} \frac{\partial \hat{H}}{\partial k_i}$ can be expressed as

$$\hat{v}_x = \frac{J\varepsilon_0}{\hbar k_0} \left(\frac{\rho}{\varepsilon_0} \right)^{\frac{J-1}{J}} \begin{pmatrix} 0 & e^{-i(J-1)\phi} \\ e^{i(J-1)\phi} & 0 \end{pmatrix}, \quad (13a)$$

$$\hat{v}_y = \frac{J\varepsilon_0}{\hbar k_0} \left(\frac{\rho}{\varepsilon_0} \right)^{\frac{J-1}{J}} \begin{pmatrix} 0 & -ie^{-i(J-1)\phi} \\ ie^{i(J-1)\phi} & 0 \end{pmatrix}, \quad (13b)$$

$$\hat{v}_z = \frac{nc_2}{\hbar k_0} \left(\frac{z}{c_2} \right)^{\frac{n-1}{n}} \begin{pmatrix} 1 & 0 \\ 0 & -1 \end{pmatrix}. \quad (13c)$$

Then the matrix elements of $M_i^{ss'}(\mathbf{k}) = \langle s, \mathbf{k} | \hbar \hat{v}_i | s', \mathbf{k} \rangle$ used in $\sigma_{xx}(\omega)$ and $\sigma_{zz}(\omega)$ are given by

$$M_x^{++}(\mathbf{k}) = \frac{J\varepsilon_0}{k_0} \left(\frac{\rho}{\varepsilon_0} \right)^{\frac{J-1}{J}} \frac{\rho \cos \phi}{E(\rho, z)}, \quad (14a)$$

$$M_x^{-+}(\mathbf{k}) = \frac{J\varepsilon_0}{k_0} \left(\frac{\rho}{\varepsilon_0} \right)^{\frac{J-1}{J}} \left[\frac{c_1 + z}{E(\rho, z)} \cos \phi - i \sin \phi \right], \quad (14b)$$

$$M_z^{++}(\mathbf{k}) = \frac{nc_2}{k_0} \left(\frac{z}{c_2} \right)^{\frac{n-1}{n}} \frac{c_1 + z}{E(\rho, z)}, \quad (14c)$$

$$M_z^{-+}(\mathbf{k}) = -\frac{nc_2}{k_0} \left(\frac{z}{c_2} \right)^{\frac{n-1}{n}} \frac{\rho}{E(\rho, z)}. \quad (14d)$$

After integrating over ρ and ϕ in Eqs. (7) and (8), we can obtain the integral expressions with respect to z for the longitudinal optical conductivity. The intraband part at zero temperature for the chemical potential $\mu \geq 0$ is then given by

$$\begin{aligned}\sigma_{xx}^{\text{intra}}(\omega) &= \frac{\pi e^2}{\hbar} \int_{z_1}^{z_2} C_n dz \int_0^\infty d\rho \int_0^{2\pi} d\phi \frac{\mathcal{J}(\rho, z)}{(2\pi)^3} |M_x^{++}(\mathbf{k})|^2 \delta(\hbar\omega) \delta(\mu - E(\rho, z)) \\ &= \frac{\pi e^2}{\hbar} \delta(\hbar\omega) \int_{z_1}^{z_2} C_n dz \int_0^\infty d\rho \frac{\mathcal{J}(\rho, z)}{(2\pi)^2} \left(\frac{J\varepsilon_0}{k_0}\right)^2 \left(\frac{\rho}{\varepsilon_0}\right)^{\frac{2(J-1)}{J}} \frac{\rho^2}{2E^2(\rho, z)} \delta(\mu - E(\rho, z)) \\ &= \frac{e^2}{\hbar} \left(\frac{Jk_0\varepsilon_0^2}{8\pi n\mu}\right) \delta(\hbar\omega) \int_{z_1}^{z_2} C_n \frac{dz}{z} \left(\frac{z}{c_2}\right)^{\frac{1}{n}} \left(\frac{\rho_\mu(z)}{\varepsilon_0}\right)^2 \Theta(\mu - |c_1 + z|),\end{aligned}\quad (15a)$$

$$\begin{aligned}\sigma_{zz}^{\text{intra}}(\omega) &= \frac{\pi e^2}{\hbar} \int_{z_1}^{z_2} C_n dz \int_0^\infty d\rho \int_0^{2\pi} d\phi \frac{\mathcal{J}(\rho, z)}{(2\pi)^3} |M_z^{++}(\mathbf{k})|^2 \delta(\hbar\omega) \delta(\mu - E(\rho, z)) \\ &= \frac{\pi e^2}{\hbar} \delta(\hbar\omega) \int_{z_1}^{z_2} C_n dz \int_0^\infty d\rho \frac{\mathcal{J}(\rho, z)}{(2\pi)^2} \left(\frac{nc_2}{k_0}\right)^2 \left(\frac{z}{c_2}\right)^{\frac{2(n-1)}{n}} \frac{(c_1 + z)^2}{E^2(\rho, z)} \delta(\mu - E(\rho, z)) \\ &= \frac{e^2}{\hbar} \left(\frac{nk_0c_2^2}{4\pi J\mu}\right) \delta(\hbar\omega) \int_{z_1}^{z_2} C_n \frac{dz}{z} \left(\frac{z}{c_2}\right)^{\frac{2n-1}{n}} \left(\frac{c_1 + z}{\varepsilon_0}\right)^2 \left(\frac{\rho_\mu(z)}{\varepsilon_0}\right)^{\frac{2(1-J)}{J}} \Theta(\mu - |c_1 + z|),\end{aligned}\quad (15b)$$

where $\rho_\mu(z) = \sqrt{\mu^2 - (c_1 + z)^2}$ and $\Theta(x)$ is the step function with $\Theta(x) = 1$ for $x > 0$ and 0 otherwise. For the integration range, $(z_1, z_2) = (-\infty, \infty)$ for odd n , $(z_1, z_2) = (0, \infty)$ for even n and $c_2 > 0$, and $(z_1, z_2) = (-\infty, 0)$ for even n and $c_2 < 0$, respectively, and $C_n = 2$ for even n and $C_n = 1$ for odd n . Here for the ρ integration with a delta function, we use the relation $\delta(f(\rho)) = \frac{1}{|f'(\rho_0)|} \delta(\rho - \rho_0)$ where $f(\rho_0) = 0$.

For the interband part of optical conductivity, we set $\mu = 0$ for simplicity. Note that non-zero μ at zero temperature only gives rise to the Pauli blocking effect, thus the effect of non-zero μ can be taken into account by introducing the step function $\Theta(\hbar\omega - 2|\mu|)$ in the $\mu = 0$ result. The interband part at zero temperature with $\mu = 0$ is given by

$$\begin{aligned}\sigma_{xx}^{\text{inter}}(\omega) &= \frac{\pi e^2}{\hbar} \int_{z_1}^{z_2} C_n dz \int_0^\infty d\rho \int_0^{2\pi} d\phi \frac{\mathcal{J}(\rho, z)}{(2\pi)^3} \frac{|M_x^{-+}(\mathbf{k})|^2}{2E(\rho, z)} \delta(\hbar\omega - 2E(\rho, z)) \\ &= \frac{\pi e^2}{\hbar} \int_{z_1}^{z_2} C_n dz \int_0^\infty d\rho \frac{\mathcal{J}(\rho, z)}{(2\pi)^2} \frac{1}{2E(\rho, z)} \left(\frac{J\varepsilon_0}{k_0}\right)^2 \left(\frac{\rho}{\varepsilon_0}\right)^{\frac{2(J-1)}{J}} \frac{1}{2} \left[\frac{(c_1 + z)^2}{E^2(\rho, z)} + 1\right] \delta(\hbar\omega - 2E(\rho, z)) \\ &= \frac{e^2}{\hbar} \left(\frac{Jk_0}{32\pi n}\right) \int_{z_1}^{z_2} C_n \frac{dz}{z} \left(\frac{z}{c_2}\right)^{\frac{1}{n}} \left[\frac{(c_1 + z)^2}{(\hbar\omega/2)^2} + 1\right] \Theta\left(\frac{\hbar\omega}{2} - |c_1 + z|\right),\end{aligned}\quad (16a)$$

$$\begin{aligned}\sigma_{zz}^{\text{inter}}(\omega) &= \frac{\pi e^2}{\hbar} \int_{z_1}^{z_2} C_n dz \int_0^\infty d\rho \int_0^{2\pi} d\phi \frac{\mathcal{J}(\rho, z)}{(2\pi)^3} \frac{|M_z^{-+}(\mathbf{k})|^2}{2E(\rho, z)} \delta(\hbar\omega - 2E(\rho, z)) \\ &= \frac{\pi e^2}{\hbar} \int_{z_1}^{z_2} C_n dz \int_0^\infty d\rho \frac{\mathcal{J}(\rho, z)}{(2\pi)^2} \frac{1}{2E(\rho, z)} \left(\frac{nc_2}{k_0}\right)^2 \left(\frac{z}{c_2}\right)^{\frac{2(n-1)}{n}} \frac{\rho^2}{E^2(\rho, z)} \delta(\hbar\omega - 2E(\rho, z)) \\ &= \frac{e^2}{\hbar} \left(\frac{nk_0}{4\pi J}\right) \left(\frac{c_2}{\hbar\omega}\right)^2 \int_{z_1}^{z_2} C_n \frac{dz}{z} \left(\frac{z}{c_2}\right)^{\frac{2n-1}{n}} \left(\frac{\rho_\omega(z)}{\varepsilon_0}\right)^{\frac{2}{J}} \Theta\left(\frac{\hbar\omega}{2} - |c_1 + z|\right),\end{aligned}\quad (16b)$$

where $\rho_\omega(z) = \sqrt{(\hbar\omega/2)^2 - (c_1 + z)^2}$. In the subsequent sections, we present calculated optical conductivity for each phase.

1. WSM phase

For the WSM phase, $c_1 = 0$, $c_2 = \hbar v_z k_0$, $c_3 = 0$ and $n = 1$. From Eqs. (15) and (16), the longitudinal optical conductivity is given by

$$\sigma_{xx}(\omega) = \frac{g_N}{24\pi} \frac{J e^2}{\hbar v_z} [4\omega_\mu^2 \delta(\omega) + \omega \Theta(\hbar\omega - 2|\mu|)], \quad (17a)$$

$$\sigma_{zz}(\omega) = \frac{g_N}{24\pi} \frac{e^2 v_z}{\hbar v_\parallel^2} \left[4A_{zz}^{\text{WSM}} \left(\frac{|\omega_\mu|}{\omega_0}\right)^{\frac{2}{J}} \omega_0^2 \delta(\omega) + B_{zz}^{\text{WSM}} \left(\frac{\omega}{\omega_0}\right)^{\frac{2}{J}-1} \omega_0 \Theta(\hbar\omega - 2|\mu|) \right], \quad (17b)$$

where $\varepsilon_0 = \hbar\omega_0 = \hbar v_{\parallel} k_0$, $\omega_{\mu} \equiv \mu/\hbar$, $A_{zz}^{\text{WSM}} = \frac{3\sqrt{\pi}\Gamma(\frac{1}{J})}{4J\Gamma(\frac{1}{J}+\frac{3}{2})}$, and $B_{zz}^{\text{WSM}} = \frac{3\sqrt{\pi}\Gamma(\frac{1}{J})}{2^{\frac{2}{J}}J^2\Gamma(\frac{1}{J}+\frac{3}{2})}$. Here we introduced the number of nodes g_N . In the derivation for σ_{zz} , we substitute $\frac{z}{\mu} = \sin\theta$ or $\frac{z}{\hbar\omega/2} = \sin\theta$, and use the relation $\int_0^{\pi/2} d\theta \cos^m\theta \sin^n\theta = \frac{1}{2}B(\frac{m+1}{2}, \frac{n+1}{2})$ where $B(m, n) = \frac{\Gamma(m)\Gamma(n)}{\Gamma(m+n)}$ is the beta function and $\Gamma(x) = \int_0^{\infty} dt t^{x-1}e^{-t}$ is the gamma function.

The first term in Eq. (17) represents the intraband transition giving rise to the Drude peak at low frequencies, whereas the second term represents interband transitions, which are forbidden at $\omega < 2|\omega_{\mu}|$ due to the Pauli blocking. For the undoped case ($\mu = 0$), the result reduces to Eq. (8) in the main text.

2. Insulator phase

For both NI and 3D QAH phases, $c_1 = \alpha$, $c_2 = \beta k_0^2$ and $n = 2$. As discussed, we set $c_3 = 0$ (or $\gamma = 0$) for simplicity. From now on, we consider only the undoped case, $\mu = 0$. The longitudinal optical conductivity is then obtained to be

$$\sigma_{xx}(\omega) = \frac{e^2}{\hbar} G_{xx}(\omega) (\hbar\omega - 2|\alpha|)^{\frac{1}{2}} \Theta(\hbar\omega - 2|\alpha|), \quad (18a)$$

$$\sigma_{zz}(\omega) = \frac{e^2}{\hbar} G_{zz}(\omega) (\hbar\omega - 2|\alpha|)^{\frac{1}{2}+\frac{3}{2}} \Theta(\hbar\omega - 2|\alpha|), \quad (18b)$$

where

$$G_{xx}(\omega) = \frac{J(16|\alpha|^2 + 4|\alpha|\hbar\omega + 9(\hbar\omega)^2)}{120\sqrt{2}\pi|\beta|^{\frac{1}{2}}(\hbar\omega)^2}, \quad (19a)$$

$$G_{zz}(\omega) = \frac{k_0\Gamma(\frac{1}{J})}{2^{\frac{2}{J}+\frac{5}{2}}\sqrt{\pi}J^2\Gamma(\frac{1}{J}+\frac{5}{2})} \frac{(|\beta|k_0^2)^{\frac{1}{2}}(\hbar\omega + 2|\alpha|)^{\frac{1}{2}}}{\varepsilon_0^{\frac{2}{J}}(\hbar\omega)^2} {}_2F_1\left(-\frac{1}{J}, \frac{3}{2}; \frac{1}{J} + \frac{5}{2}; \frac{2|\alpha| - \hbar\omega}{2|\alpha| + \hbar\omega}\right), \quad (19b)$$

and ${}_2F_1(a, b; c; z) = \frac{\Gamma(c)}{\Gamma(b)\Gamma(c-b)} \int_0^1 dt \frac{t^{b-1}(1-t)^{c-b-1}}{(1-tz)^a}$ is the hypergeometric function. Note that the analytic expressions for the longitudinal conductivities with $\gamma = 0$ have the same form for both NI and 3D QAH phases except for the sign of α : $\alpha > 0$ for the NI and $\alpha < 0$ for the 3D QAH phase.

3. Transition point

For the transition point between the WSM and NI phases or between the WSM and 3D QAH phases, the analytical results can be obtained by taking the limit $\alpha \rightarrow 0$ in Eq. (18):

$$\sigma_{xx}(\omega) = \frac{e^2}{\hbar} A_{xx} (\hbar\omega)^{\frac{1}{2}}, \quad (20a)$$

$$\sigma_{zz}(\omega) = \frac{e^2}{\hbar} A_{zz} (\hbar\omega)^{\frac{2}{J}-\frac{1}{2}}, \quad (20b)$$

where

$$A_{xx} = \frac{3J}{40\sqrt{2}\pi|\beta|^{\frac{1}{2}}}, \quad (21a)$$

$$A_{zz} = \frac{k_0\Gamma(\frac{1}{J})(|\beta|k_0^2)^{\frac{1}{2}}}{2^{\frac{2}{J}+2}J^2\Gamma(\frac{1}{4})\Gamma(\frac{1}{J}+\frac{7}{4})\varepsilon_0^{\frac{2}{J}}}. \quad (21b)$$

Here we used ${}_2F_1(a, b; c; z) = {}_2F_1(b, a; c; z)$, ${}_2F_1(a, b; 1+a-b; -1) = \frac{\Gamma(1+a-b)\Gamma(1+\frac{1}{2}a)}{\Gamma(1+a)\Gamma(1+\frac{1}{2}a-b)}$, and $\Gamma(x)\Gamma(1-x) = \frac{\pi}{\sin \pi x}$.

B. Transverse optical conductivity

From Eq. (7) in the main text, the Hall or transverse optical conductivity σ_{xy} for $\mu = 0$ is given by

$$\sigma_{xy}(\omega) = -\frac{ie^2}{\hbar} \int \frac{d^3k}{(2\pi)^3} \frac{f_{+, \mathbf{k}} - f_{-, \mathbf{k}}}{\varepsilon_{+, \mathbf{k}} - \varepsilon_{-, \mathbf{k}}} \left[\frac{M_x^{+-}(\mathbf{k})M_y^{-+}(\mathbf{k})}{\hbar\omega + \varepsilon_{+, \mathbf{k}} - \varepsilon_{-, \mathbf{k}}} + \frac{M_x^{-+}(\mathbf{k})M_y^{+-}(\mathbf{k})}{\hbar\omega + \varepsilon_{-, \mathbf{k}} - \varepsilon_{+, \mathbf{k}}} \right]. \quad (22)$$

Here, in contrast to the longitudinal optical conductivity, we keep c_3 (or γ) for analytic expressions. Throughout this section, for brevity, the momentum and the energy are normalized by k_0 and ε_0 , respectively, or equivalently we set $k_0 = \varepsilon_0 = 1$.

We consider the following coordinate transformation:

$$\begin{aligned} k_x &\rightarrow \rho^{\frac{1}{J}} \cos \phi, \\ k_y &\rightarrow \rho^{\frac{1}{J}} \sin \phi, \\ k_z &\rightarrow k_z, \end{aligned} \quad (23)$$

whose Jacobian is given by

$$\mathcal{J} = \frac{\rho^{\frac{2}{J}-1}}{J} \equiv \mathcal{J}(\rho). \quad (24)$$

In the transformed coordinate, the Hamiltonian becomes

$$H = \rho(e^{-iJ\phi}\sigma_+ + e^{iJ\phi}\sigma_-) + (c_1 + c_2q_z^n + c_3\rho^{\frac{2}{J}})\sigma_z \quad (25)$$

and the energy dispersion is given by $E_{\pm}(\rho, q_z) = \pm E(\rho, q_z)$ where

$$E(\rho, q_z) = \sqrt{\rho^2 + \left(c_1 + c_2q_z^n + c_3\rho^{\frac{2}{J}}\right)^2}. \quad (26)$$

The corresponding eigenstate is given by

$$|+; \rho, \phi, q_z\rangle = \begin{pmatrix} \cos \frac{\theta}{2} \\ \sin \frac{\theta}{2} e^{iJ\phi} \end{pmatrix}, \quad (27a)$$

$$|-; \rho, \phi, q_z\rangle = \begin{pmatrix} -\sin \frac{\theta}{2} \\ \cos \frac{\theta}{2} e^{iJ\phi} \end{pmatrix}, \quad (27b)$$

where $\theta = \tan^{-1}\left(\frac{\rho}{m(\rho, q_z)}\right)$ and $m(\rho, q_z) = c_1 + c_2q_z^n + c_3\rho^{\frac{2}{J}}$. Note that $\cos \theta = \frac{m(\rho, q_z)}{E(\rho, q_z)}$ and $\sin \theta = \frac{\rho}{E(\rho, q_z)}$.

The velocity matrices $\hat{v}_i = \frac{1}{\hbar} \frac{\partial \hat{H}}{\partial k_i}$ can be expressed as

$$\hat{v}_x = \frac{1}{\hbar} \begin{pmatrix} 2c_3\rho^{\frac{1}{J}} \cos \phi & J\rho^{\frac{J-1}{J}} e^{-i(J-1)\phi} \\ J\rho^{\frac{J-1}{J}} e^{i(J-1)\phi} & -2c_3\rho^{\frac{1}{J}} \cos \phi \end{pmatrix}, \quad (28a)$$

$$\hat{v}_y = \frac{1}{\hbar} \begin{pmatrix} 2c_3\rho^{\frac{1}{J}} \sin \phi & -iJ\rho^{\frac{J-1}{J}} e^{-i(J-1)\phi} \\ iJ\rho^{\frac{J-1}{J}} e^{i(J-1)\phi} & -2c_3\rho^{\frac{1}{J}} \sin \phi \end{pmatrix}. \quad (28b)$$

Then the matrix elements of $M_i^{ss'}(\mathbf{k}) = \langle s, \mathbf{k} | \hbar \hat{v}_i | s', \mathbf{k} \rangle$ used in $\sigma_{xy}(\omega)$ are given by

$$M_x^{+-}(\mathbf{k}) = J \left[\rho^{\frac{J-1}{J}} (\cos \theta \cos \phi + i \sin \phi) \right] - 2c_3\rho^{\frac{1}{J}} \sin \theta \cos \phi, \quad (29a)$$

$$M_y^{-+}(\mathbf{k}) = J \left[\rho^{\frac{J-1}{J}} (\cos \theta \sin \phi + i \cos \phi) \right] - 2c_3\rho^{\frac{1}{J}} \sin \theta \sin \phi. \quad (29b)$$

Note that

$$\int_0^{2\pi} \frac{d\phi}{2\pi} M_x^{+-}(\mathbf{k}) M_y^{-+}(\mathbf{k}) = \int_0^{2\pi} \frac{d\phi}{2\pi} (M_x^{-+}(\mathbf{k}) M_y^{+-}(\mathbf{k}))^* = iJ^2 \rho^{\frac{2(J-1)}{J}} \left[\frac{J(c_1 + c_2q_z^n) + (J-2)c_3\rho^{\frac{2}{J}}}{E(\rho, q_z)} \right]. \quad (30)$$

Then from Eq. (22) the real part of the transverse optical conductivity is given by

$$\begin{aligned} \sigma_{xy}(\omega) &= -\frac{ie^2}{\hbar} \int_0^\infty d\rho \int_{-k_c}^{k_c} dk_z \int_0^{2\pi} d\phi \frac{\mathcal{J}(\rho)}{(2\pi)^3} \frac{1}{2E(\rho, q_z)} \left[\frac{M_x^{+-}(\mathbf{k}) M_y^{-+}(\mathbf{k})}{\hbar\omega + 2E(\rho, q_z)} + \frac{M_x^{-+}(\mathbf{k}) M_y^{+-}(\mathbf{k})}{\hbar\omega - 2E(\rho, q_z)} \right] \\ &= -\frac{e^2}{\hbar} \frac{1}{8\pi^2} \int_0^\infty \rho d\rho \int_{-k_c}^{k_c} dk_z \left[\frac{J(c_1 + c_2q_z^n) + (J-2)c_3\rho^{\frac{2}{J}}}{E(\rho, q_z)} \right] \left[\frac{1}{E^2(\rho, q_z) - (\hbar\omega/2)^2} \right]. \end{aligned} \quad (31)$$

Here we introduce the momentum cutoff k_c along the k_z direction to prevent divergence of the integral. Using these results, we can obtain the real part of the transverse optical conductivity up to second order in ω as $\sigma_{xy}(\omega) \approx \sigma_{xy}^{(0)} + \sigma_{xy}^{(2)}(\omega)$, where

$$\begin{aligned}\sigma_{xy}^{(0)} &= -\frac{e^2}{\hbar} \frac{1}{8\pi^2} \int_{-k_c}^{k_c} dk_z \int_0^\infty \rho d\rho \frac{J(c_1 + c_2 q_z^n) + (J-2)c_3 \rho^{\frac{2}{J}}}{E^3(\rho, q_z)} \\ &= \frac{e^2}{\hbar} \frac{1}{8\pi^2} \int_{-k_c}^{k_c} dk_z \frac{J(c_1 + c_2 q_z^n + c_3 \rho^{\frac{2}{J}})}{E(\rho, q_z)} \bigg|_{\rho \rightarrow 0}^{\rho \rightarrow \infty},\end{aligned}\quad (32a)$$

$$\sigma_{xy}^{(2)}(\omega) = -\frac{e^2}{\hbar} \frac{(\hbar\omega)^2}{32\pi^2} \int_{-k_c}^{k_c} dk_z \int_0^\infty \rho d\rho \frac{J(c_1 + c_2 q_z^n) + (J-2)c_3 \rho^{\frac{2}{J}}}{E^5(\rho, q_z)}.\quad (32b)$$

From now on, we recover k_0 and ε_0 for clarity.

1. WSM phase

For the WSM phase, $c_1 = 0$, $c_2 = \hbar v_z k_0$, $c_3 = 0$ and $n = 1$. Then the Hall conductivity for a single Weyl node is given by

$$\sigma_{xy}^{(0)} = -\frac{e^2}{\hbar} \frac{J}{8\pi^2} \int_{-k_c}^{k_c} dk_z \text{sgn}(v_z q_z).\quad (33)$$

Note that there always appear multiple Weyl points in the Brillouin zone with the total chirality sum zero. Here we consider the simplest case in which two Weyl nodes with opposite chirality are located at $\pm b\hat{z}$, respectively. Assuming that the node with positive chirality is at $k_z = +b\hat{z}$ and the negative one at $k_z = -b\hat{z}$ with $|b| < k_c$, we find

$$\sigma_{xy}^{(0)} = -\frac{e^2}{\hbar} \frac{J}{8\pi^2} \int_{-k_c}^{k_c} dk_z \{ \text{sgn}[v_z(k_z - b)] + \text{sgn}[(-v_z)(k_z + b)] \}\quad (34)$$

$$= J \frac{e^2}{\hbar} \frac{b}{\pi}.\quad (35)$$

Here the first and second terms in the first line represent contributions from the positive and negative chirality nodes, respectively.

Similarly, we can obtain the dynamical part of the Hall conductivity. For a single Weyl node,

$$\begin{aligned}\sigma_{xy}^{(2)}(\omega) &= -\frac{e^2}{\hbar} \frac{J(\hbar\omega)^2}{32\pi^2} \int_{-k_c}^{k_c} dk_z \int_0^\infty \rho d\rho \frac{\hbar v_z q_z}{[\rho^2 + (\hbar v_z q_z)^2]^{\frac{5}{2}}} \\ &= -\frac{e^2}{\hbar} \frac{J(\hbar\omega)^2}{96\pi^2} \int_{-k_c}^{k_c} dk_z \frac{\text{sgn}(v_z q_z)}{(\hbar v_z q_z)^2}.\end{aligned}\quad (36)$$

Then the total conductivity contributed from the two Weyl nodes is given by

$$\begin{aligned}\sigma_{xy}^{(2)}(\omega) &= -\frac{e^2}{\hbar} \frac{J\omega^2}{96\pi^2 v_z^2} \int_{-k_c}^{k_c} dk_z \left\{ \frac{\text{sgn}[v_z(k_z - b)]}{(k_z - b)^2} + \frac{\text{sgn}[(-v_z)(k_z + b)]}{(k_z + b)^2} \right\} \\ &= \frac{e^2}{\hbar} \frac{J}{24\pi^2 v_z^2} \frac{b}{k_c^2 - b^2} \omega^2.\end{aligned}\quad (37)$$

2. Insulator phase

For both NI and 3D QAH phases, $c_1 = \alpha$, $c_2 = \beta k_0^2$, $c_3 = \gamma k_0^2$ and $n = 2$. The static part of the Hall conductivity after the integration over ρ is given by

$$\sigma_{xy}^{(0)} = \frac{e^2}{\hbar} \frac{1}{8\pi^2} \int_{-k_c}^{k_c} dk_z \begin{cases} 1 - \text{sgn}[f(q_z)] & (J = 1), \\ \frac{2\gamma k_0^2}{\sqrt{(\gamma k_0^2)^2 + \varepsilon_0^2}} - 2\text{sgn}[f(q_z)] & (J = 2), \end{cases}\quad (38)$$

where $f(q_z) = \alpha + \beta q_z^2$. Now, the integral is straightforward. In the NI phase ($\alpha > 0, \beta > 0$), $\text{sgn}[f(q_z)] = 1$ thus

$$\sigma_{xy}^{(0)} = \frac{e^2}{\hbar} \begin{cases} 0 & (J = 1), \\ \frac{k_c}{2\pi^2} \left(\frac{\gamma k_0^2}{\sqrt{(\gamma k_0^2)^2 + \varepsilon_0^2}} - 1 \right) & (J = 2), \end{cases} \quad (39)$$

whereas in the 3D QAH phase ($\alpha < 0, \beta < 0$), $\text{sgn}[f(q_z)] = -1$ thus

$$\sigma_{xy}^{(0)} = \frac{e^2}{\hbar} \begin{cases} \frac{k_c}{2\pi^2} & (J = 1), \\ \frac{k_c}{2\pi^2} \left(\frac{\gamma k_0^2}{\sqrt{(\gamma k_0^2)^2 + \varepsilon_0^2}} + 1 \right) & (J = 2). \end{cases} \quad (40)$$

Similarly, we can obtain the dynamical part of the Hall conductivity. In the NI phase,

$$\sigma_{xy}^{(2)} = \frac{e^2}{\hbar} k_0 \left(\frac{\hbar\omega}{\varepsilon_0} \right)^2 \begin{cases} -\frac{k_c \varepsilon_0^2}{96\pi^2 \alpha k_0 (\alpha + \beta k_c^2)} + \frac{8\alpha \gamma k_0^2 - \varepsilon_0^2}{96\pi^2 \sqrt{\alpha^3 \beta} k_0} \tan^{-1} \left(\sqrt{\frac{\beta}{\alpha}} k_c \right) - \frac{\gamma k_0^2 \tan^{-1} \left[2\sqrt{\frac{\beta k_c^2 \gamma k_0^2}{4\alpha \gamma k_0^2 + \varepsilon_0^2}} \right]}{6\pi^2 \sqrt{\frac{\beta(4\alpha \gamma k_0^2 + \varepsilon_0^2)}{\gamma}}} & (J = 1), \\ \frac{\gamma k_0^2 \varepsilon_0}{24\pi^2 \alpha^2 (\alpha + \beta k_c^2)} \sqrt{\frac{\alpha(\gamma^2 k_0^4 + \varepsilon_0^2)}{\beta k_0^2 \varepsilon_0^2}} \left[\tan^{-1} \left(\sqrt{\frac{\beta}{\alpha}} k_c \right) (\alpha + \beta k_c^2) - k_c \sqrt{\alpha \beta} \right] & (J = 2), \end{cases} \quad (41)$$

whereas in the 3D QAH phase,

$$\sigma_{xy}^{(2)} = \frac{e^2}{\hbar} k_0 \left(\frac{\hbar\omega}{\varepsilon_0} \right)^2 \begin{cases} \frac{k_c \varepsilon_0^2}{96\pi^2 k_0 \alpha (\alpha + \beta k_c^2)} - \frac{8\alpha \gamma k_0^2 - \varepsilon_0^2}{96\pi^2 \sqrt{\alpha^3 \beta} k_0} \tan^{-1} \left(\sqrt{\frac{\beta}{\alpha}} k_c \right) & (J = 1), \\ \frac{\gamma k_0^2 \varepsilon_0}{24\pi^2 \alpha^2 (\alpha + \beta k_c^2)} \sqrt{\frac{\alpha(\gamma^2 k_0^4 + \varepsilon_0^2)}{\beta k_0^2 \varepsilon_0^2}} \left[\tan^{-1} \left(\sqrt{\frac{\beta}{\alpha}} k_c \right) (\alpha + \beta k_c^2) - k_c \sqrt{\alpha \beta} \right] & (J = 2). \end{cases} \quad (42)$$

Note that for $J = 2$, the dynamical part for the 3D QAH phase is given by the same form as that for the NI phase.

3. Transition point

For the transition point between the WSM and NI phases or between the WSM and 3D QAH phases, $c_1 = 0$, $c_2 = \beta k_0^2$, $c_3 = \gamma k_0^2$ and $n = 2$. Then the transverse optical conductivity is given by the following form:

$$\sigma_{xy}^{\text{NI}}(\omega) = \frac{e^2}{\hbar} [A_{xy}^{\text{NI}} + B_{xy} \omega^\nu], \quad (43a)$$

$$\sigma_{xy}^{\text{QAH}}(\omega) = \frac{e^2}{\hbar} \left[\frac{J k_c}{2\pi^2} + A_{xy}^{\text{NI}} + B_{xy} \omega^\nu \right], \quad (43b)$$

where A_{xy}^{NI} is a residual conductivity for the NI phase given by $A_{xy}^{\text{NI}}|_{J=1} = 0$ for $J = 1$ and $A_{xy}^{\text{NI}}|_{J=2} = \frac{k_c}{2\pi^2} \left(\frac{\gamma k_0^2}{\sqrt{(\gamma k_0^2)^2 + \varepsilon_0^2}} - 1 \right)$ for $J = 2$, as seen in Eq. (39). Here the exponent $\nu \approx 0.5$ is found numerically from Eq. (31) for $J = 1, 2$ with a frequency independent coefficient B_{xy} .